

Chapter 5

3D data examples

In this chapter I will demonstrate the effectiveness of the methodologies developed in the previous chapters using 3D data examples. I will first show inversion results of a realistically complex synthetic model. Then I will show inversion results of onshore field data.

REALISTICALLY COMPLEX SYNTHETIC INVERSION

Modeling generation and survey design

The realistic velocity model is generated by simulating a sequence a series of geological processes (Clapp, 2013). The most frequently simulated geological process is deposit, which is implemented as depositing a layer of constant thickness velocity onto the top of the current model. Depositing layers create a simple model that can be made more complex. More specifically, the simple model can be made more complex by simulating certain “morphing” processes such as uplift, compact and faulting. Those simulated geological processes create long-wavelength velocity structures, short wavelength velocity structures are created by inserting thin layers of varying thickness and varying velocity values in the deposited layers, as well as simulating the erosion process. The simulated erosion process create thin meandering channels in the model.

The true model created by the combination of all those processes is realistically complicated (Figure 5.1). Physically, the true model is 4 km in both lateral directions, and 1.5 km in depth.

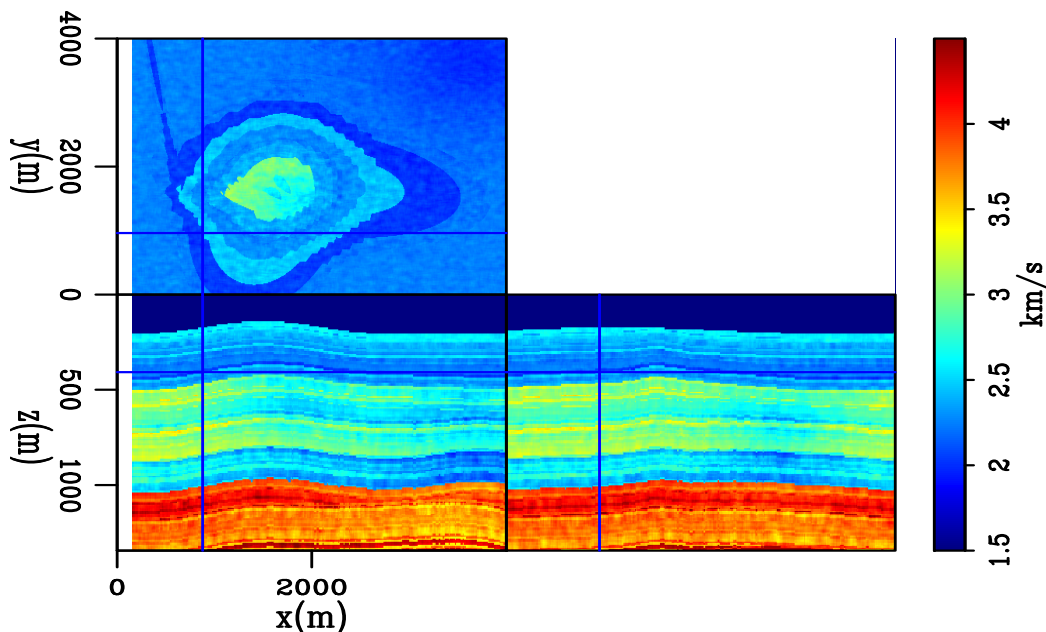


Figure 5.1: True velocity model for tomography. [NR] chap5/. vtrue

The starting model (Figure 5.2) is far from the true model, to test the capability of the methodologies developed in the previous chapters. Firstly, the long wavelength velocity components are wrong in the starting model. The dips of most structures are wrong by a significant amount. Furthermore, there are large, slow velocity anomalies in the starting model which do not exist in the true model, and vice versa. Secondly, the starting model is very smooth, i.e., does not contain any short wavelength velocity structure. The lack of the short-wavelength structures are a combination of not incorporating the corresponding geological processes during the model creation and a subsequent heavy smoothing operation of the created model.

The realistically complex true model and extremely smooth starting model are frequently encountered in field data inversions. In addition to these, observed data are created with realistic acquisition geometry. The synthetic acquisition geometry

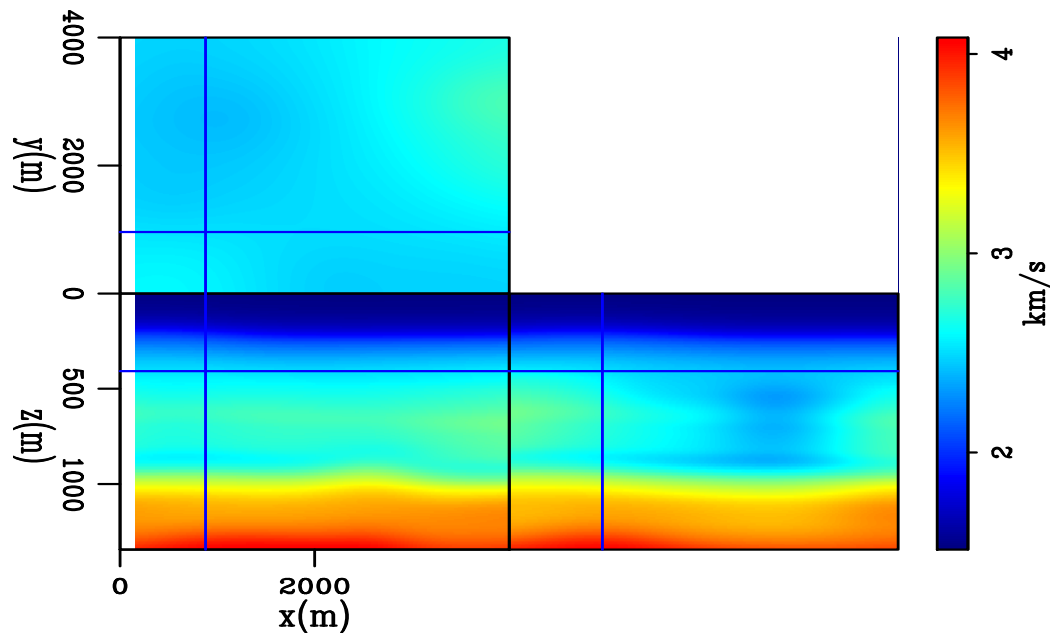


Figure 5.2: Starting velocity model for tomography. [NR] chap5/. vinit

incorporated important aspects of field data acquisition geometry used in the real data inversion example later in this chapter. The sources fall on a regular grid of 24m spacing in x and 24m spacing in y . However, sources do not exist on all the grid points, in order to simulate realistic surveys where missing sources are not uncommon. In certain areas of the survey, sources are completely absent. In addition to that, missing source locations are randomly dispersed throughout the survey area. The receivers are on a regular grid of 24m spacing in x and 192m spacing in y . The dataset was generated with a constant density, two-way acoustic wave equation engine. A Ricker wavelet was used as the source wavelet, and these modeled data were band-passed between 5 Hz and 62.5 Hz. The band-pass operation simulates the lack of low-frequency data that is common in the real data inversion applications.

Tomography and results

The aforementioned realistic acquisition geometry determines two important aspects of the inversion. Firstly, the geometry determines the offset distribution of the dataset (Figure 5.3). Although the maximum offset is at 3.5 km, data with such offset does not constitute a large portion of the entire dataset. Such distribution of offset ranges limit the capability of the inversions to resolve deep structures in the near-surface model. Secondly, the geometry resulted in fewer receiver gathers than shot gathers. Hence, in the inversion, data modeling and matching are carried out on receiver gathers for computational efficiency. In the following part of the section, receiver gathers will be called shot gathers.

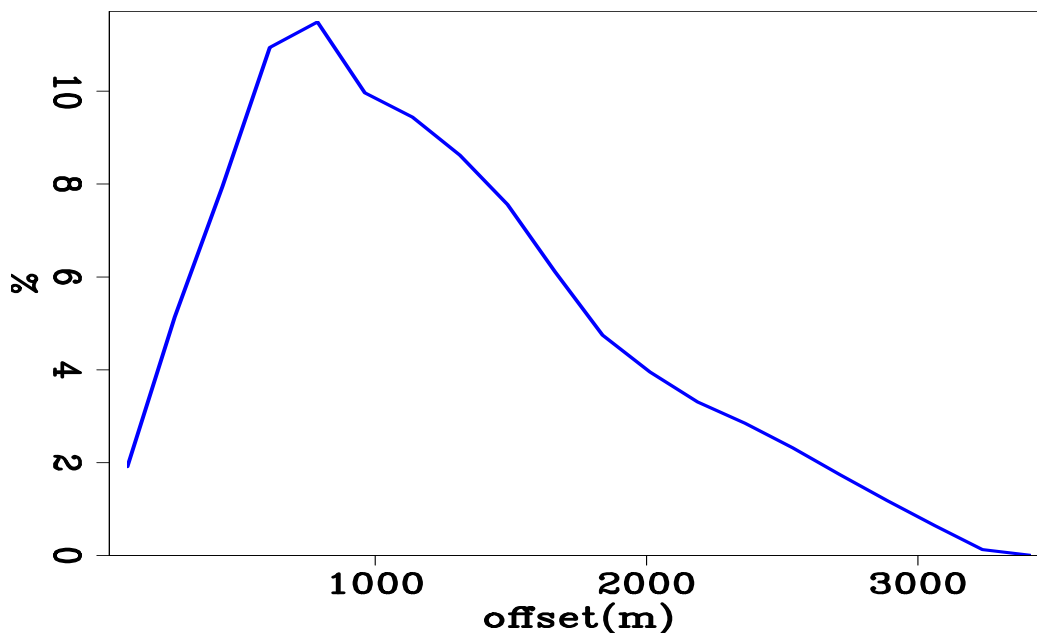


Figure 5.3: Histogram of source-receiver offset distribution in the dataset. [NR]
`chap5/. hhist`

As mentioned before, the long-wavelength components of the initial model have significant errors. As a result, for the traveltimes inversion, the data was low-passed at 10Hz to attempt to correct the long-wavelength errors. In addition, only first-breaks are used. For the kinematic waveform inversion in which the main purpose is to

recover the short-wavelength components, all the data are used, and three successive stages of inversion are performed with input data low-passed at 10Hz, 17Hz and no low-pass at all (Figure 5.4). I will first discuss the traveltimes inversion result, then I will present the kinematic waveform inversion results.

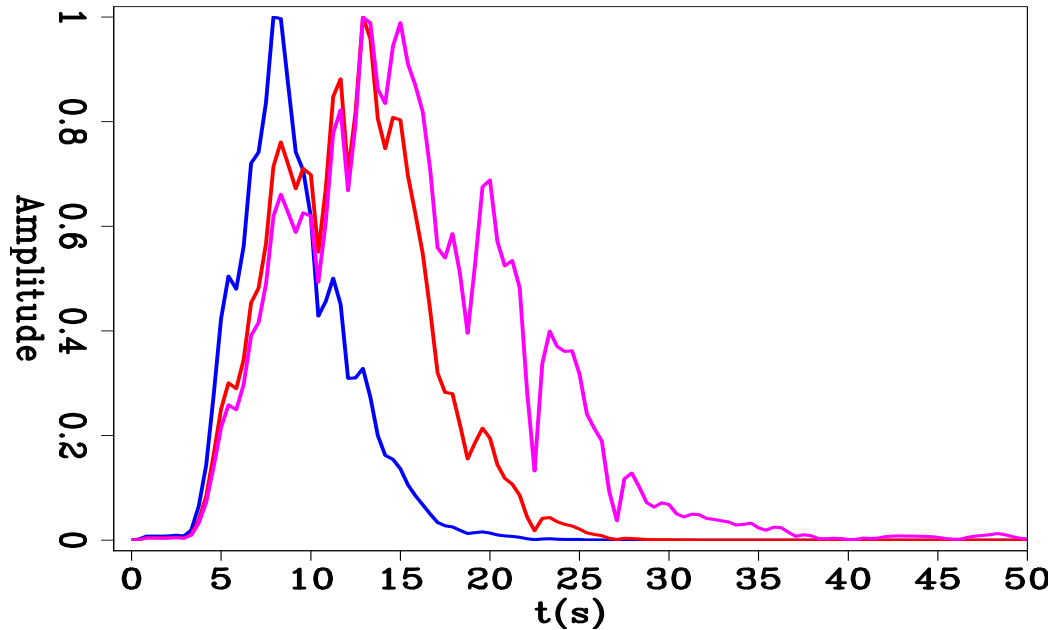


Figure 5.4: Spectrum of input data with 10Hz low-pass, 17Hz low-pass and no band-pass at all. [NR] chap5/. syndspectr

A total of 11 iterations of wave-equation traveltimes inversion were run. The initial traveltimes residual was significantly reduced, especially in the far offset where the initial first-break traveltimes difference between the observed first-breaks and modeled first-breaks is greater than 0.2 s (Figure 5.6), which is more than a half cycle of the wavelet (Figure 5.5). Some of missing long-wavelength structures such as the uplift centered at 1.5 km in both horizontal directions start to appear in the traveltimes inversion result (Figure 5.7). On the other hand, since short-wavelength components can not be resolved by the traveltimes inversion, the result is still very smooth compared with the true model. As shown before (Figure 5.3), data with relatively long offset is only a small portion of the entire dataset, it is important to quantify the depth to which first-break traveltimes inversion is capable of resolving.

This is very important for evaluating the subsequent kinematic waveform inversion results. Since beyond such depth, the errors in the long-wavelength components are not corrected by the traveltimes inversion, leaving no chance for kinematic waveform inversion to converge to the true model. As shown by the first-break traveltimes inversion gradient of a single data trace, which has the typical ‘long-offset’ in the dataset (Figure 5.8), the first-break traveltimes inversion only corrects long-wavelength velocity errors down to 1 km. In other words, the offset of the dataset limits the illumination of the first-break traveltimes inversion, which in turn limits the depth to which the traveltimes inversion is capable of resolving. In addition, the limited illumination of first-breaks give rise to the increased inaccuracy of the inversion results towards the boundaries of the model.

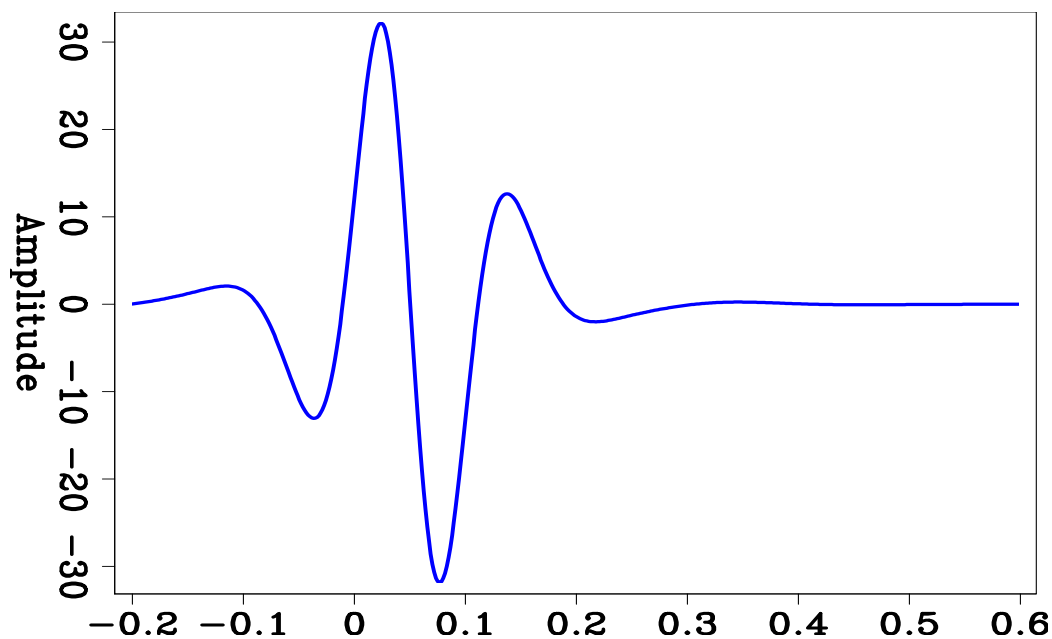


Figure 5.5: Time domain source wavelet for first-break wave-equation traveltimes inversion. [NR] `chap5/. waveletWT`

Three stages of successive kinematic waveform inversion were run using all the data (including reflections), with increasing frequency content, the result of each stage was used as the starting model for the next stage. The first inversion with 10Hz low-pass data had a total of 18 iterations. The second inversion with 17Hz low-pass

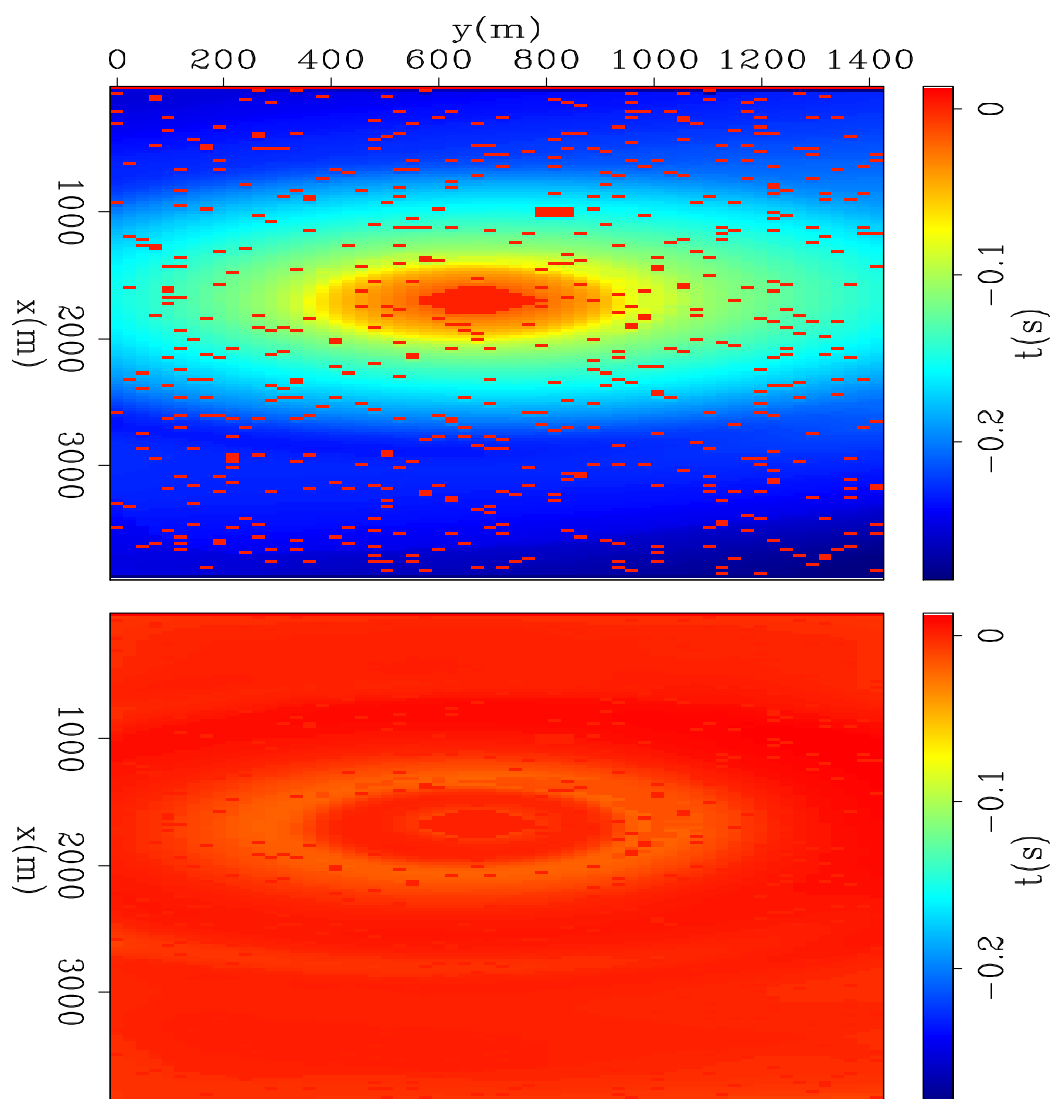


Figure 5.6: First-break traveltime residual for a shot gather before (top) and after (bottom) wave-equation traveltime inversion. The large initial traveltime residuals at the far offset indicate cycle-skipping. Red dots are locations with missing traces.

[CR] chap5/. wtdres

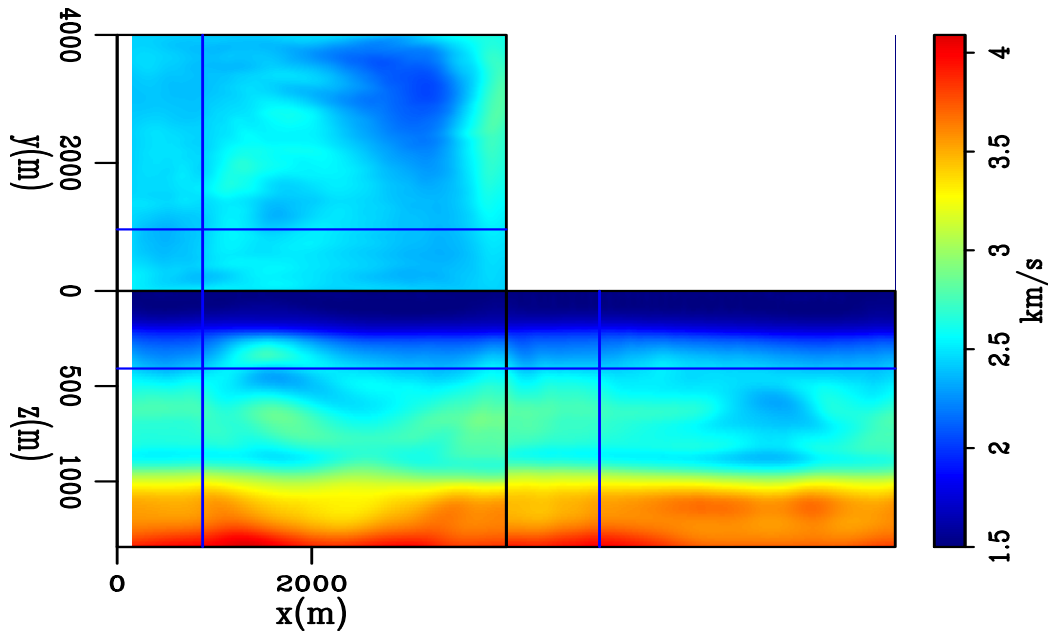


Figure 5.7: First-break wave-equation traveltime inversion result. [CR]

chap5/.vinvwt

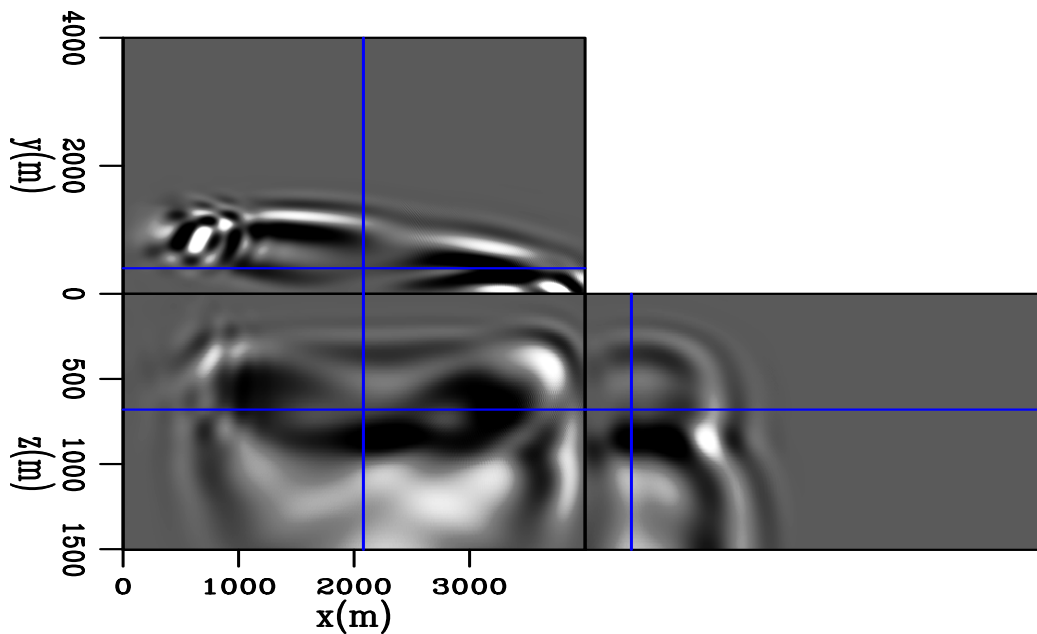


Figure 5.8: Gradient of a single source-receiver pair. Notice the limited depth penetration even with the long off-set. [CR] chap5/.srgrad

data had a total of 12 iterations. The third inversion with no band-pass had a total of 22 iterations. The difference in iteration numbers is mainly due to the different steplength used in each inversion stage. Higher frequency data leads to a higher resolution result (Figure 5.9, Figure 5.10 and Figure 5.11), the final velocity model after three inversion stages has sufficiently high resolution that fine velocity structures such as thin channels are evident. The thin channel of low-velocity is recovered only after the third inversion stage because only the data before band-pass contains the reflections from the top and bottom of the thin channel (Figure 5.12). Conversely, the kinematic waveform inversions failed to converge to the true model below 1 km, where the first-break traveltimes inversion failed to update the initial model. However, given the good near-surface model obtained with the workflow, velocity errors below 1 km can be corrected with other tomography methods, such as rms velocity analysis and/or reflection tomography.

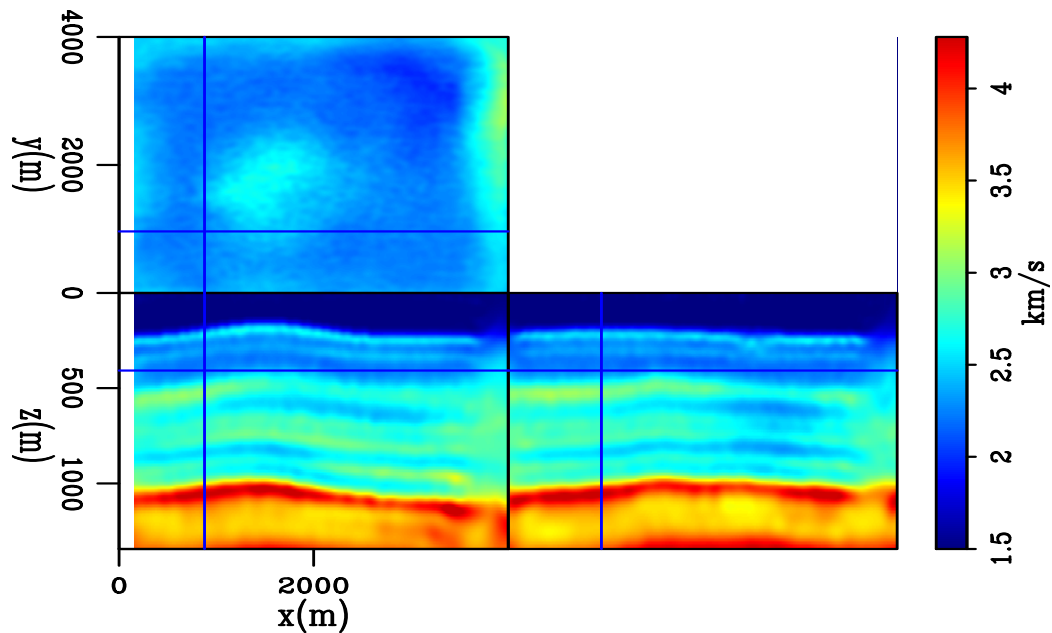


Figure 5.9: Kinematic waveform inversion using 10Hz low-pass data. [CR]
 chap5/.vinvwil

In addition to comparing final inversion results to the true model, a data residual map also gives important information regarding the inversion result. The shot gather

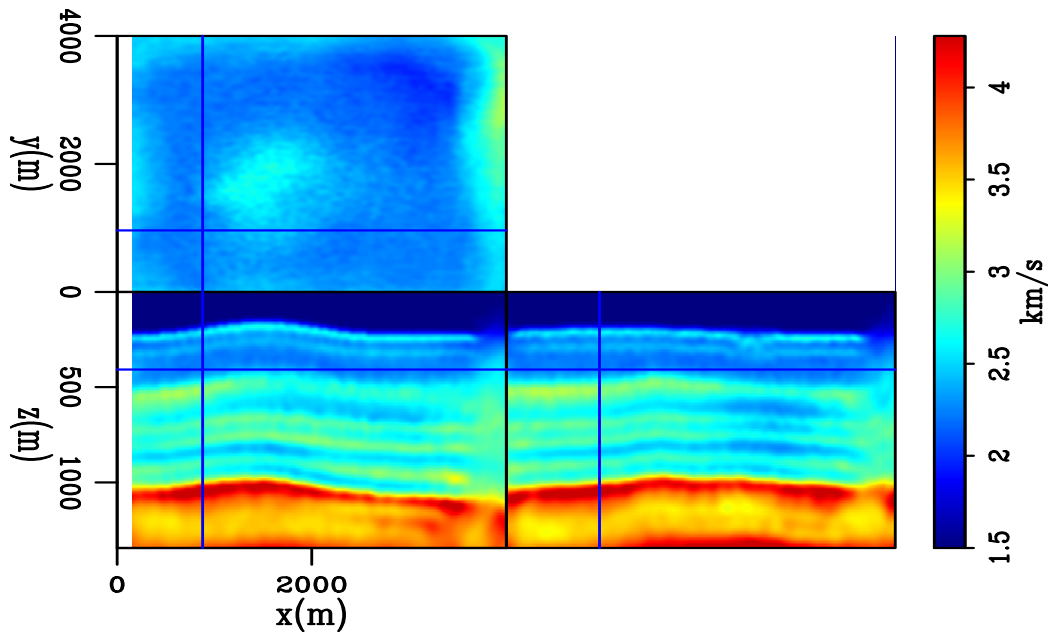


Figure 5.10: Kinematic waveform inversion using 17Hz low-pass data. [CR]

chap5/.vinvwim

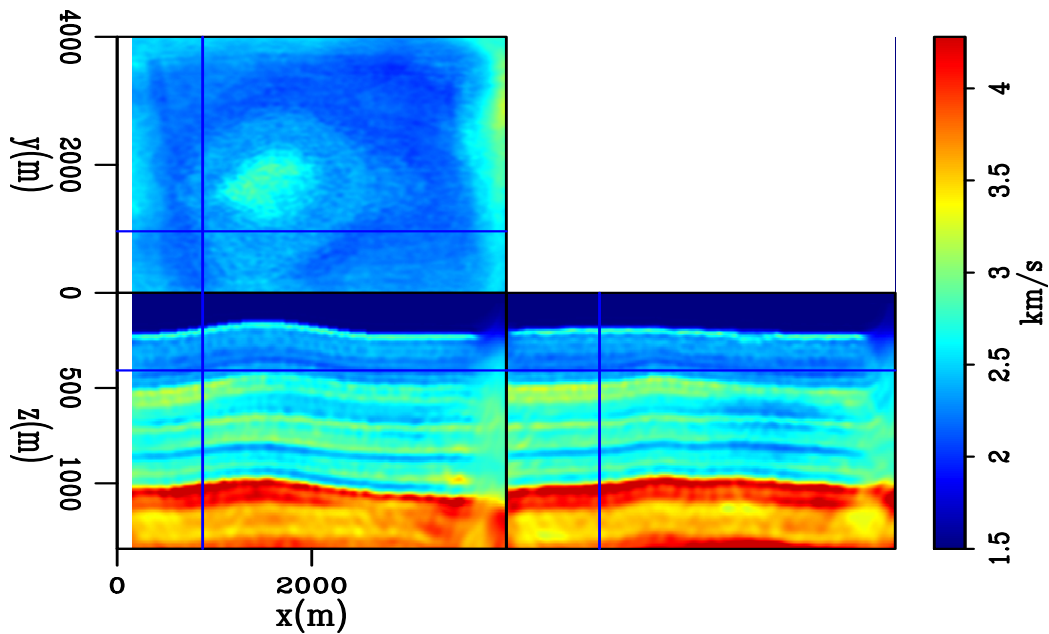


Figure 5.11: Kinematic waveform inversion using data without band-pass. [CR]

chap5/.vinvwih

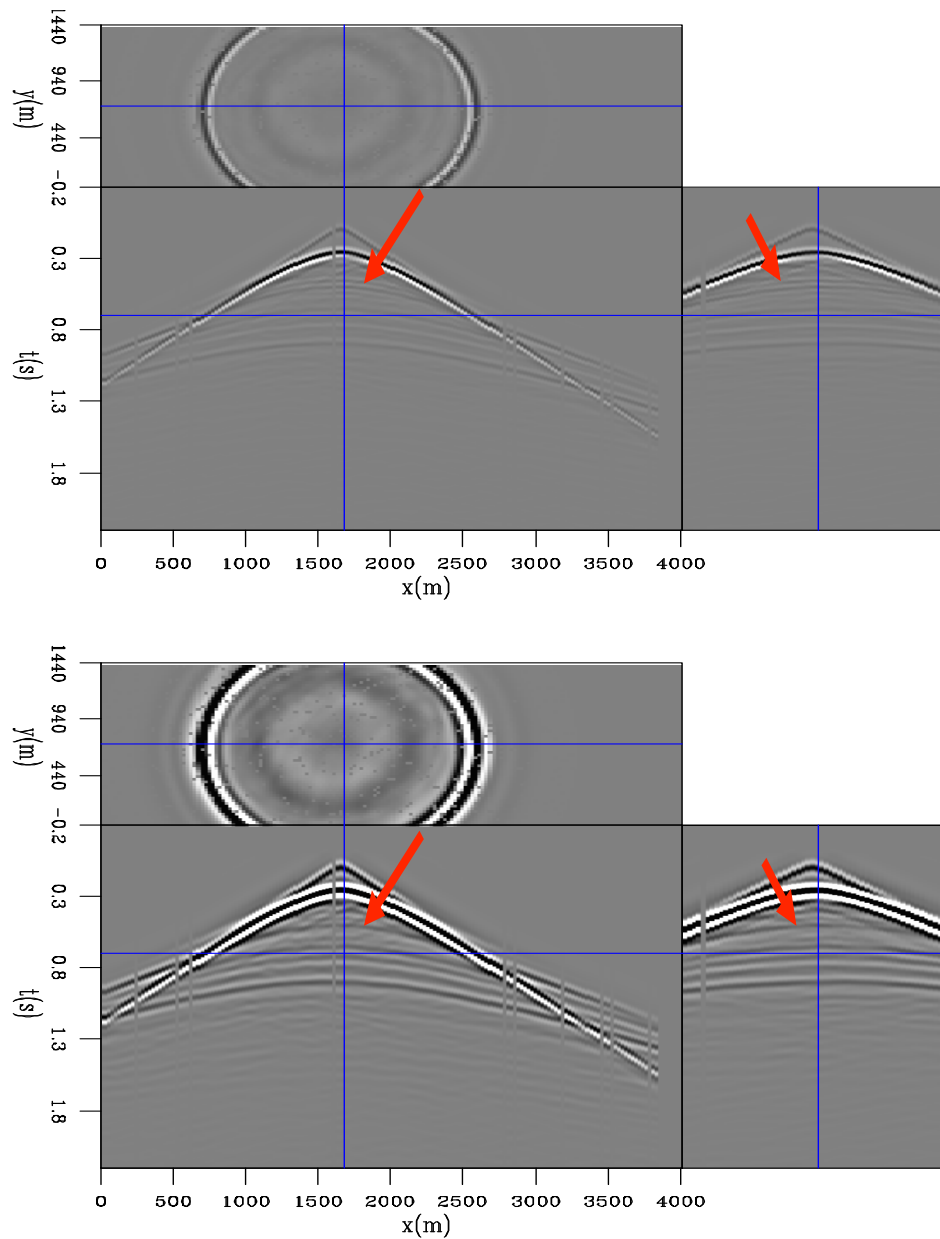


Figure 5.12: input shot gather with 17Hz low-pass and no band-pass, reflections from the thin channel are denoted by the red arrows. Data with no band-pass has both top and bottom reflections of the thin channel, while data with 17Hz low-pass does not have such resolution. [CR] chap5/. thinchandcomp

residual map (Figure 5.13) suggests that the kinematic waveform inversion struggles near the boundary of the model. Since the first-break traveltime inversion cannot correct for long-wavelength model errors near the boundary (due to the spatial illuminations of the first-breaks), the subsequent kinematic waveform inversion can not correctly update the short-wavelength components near the boundaries, leaving large data residuals. For shot gathers far from the boundary regions, these data residuals are very small. A typical shot gather residual (Figure 5.14), when compared with the observed data (Figure 5.15) and the modeled data (Figure 5.16), shows that the major data residual, although weak compared with the modeled and observed data, is the mismatch of first interface reflections and direct arrivals. These two events are only determined by the velocity of the first layer. However, the calculated gradients from cross-correlation of the source wavefield and residual wavefield have non-zero values in the first layer even when the first layer velocity is correct. Cumulatively, these non-zero-values in the gradients leave artifacts in the first layer velocity (Figure 5.17) and causes strong residual of the direct arrivals and first interface reflections. Such artifacts can potentially be mitigated by running joint inversion of early-arrivals and first-break traveltimes. Furthermore, joint inversion of first-break traveltime and early-arrival waveforms with proper weighting coefficient enables us to incorporate the two-step workflow into one-step and potentially better constrain the inverse problem.

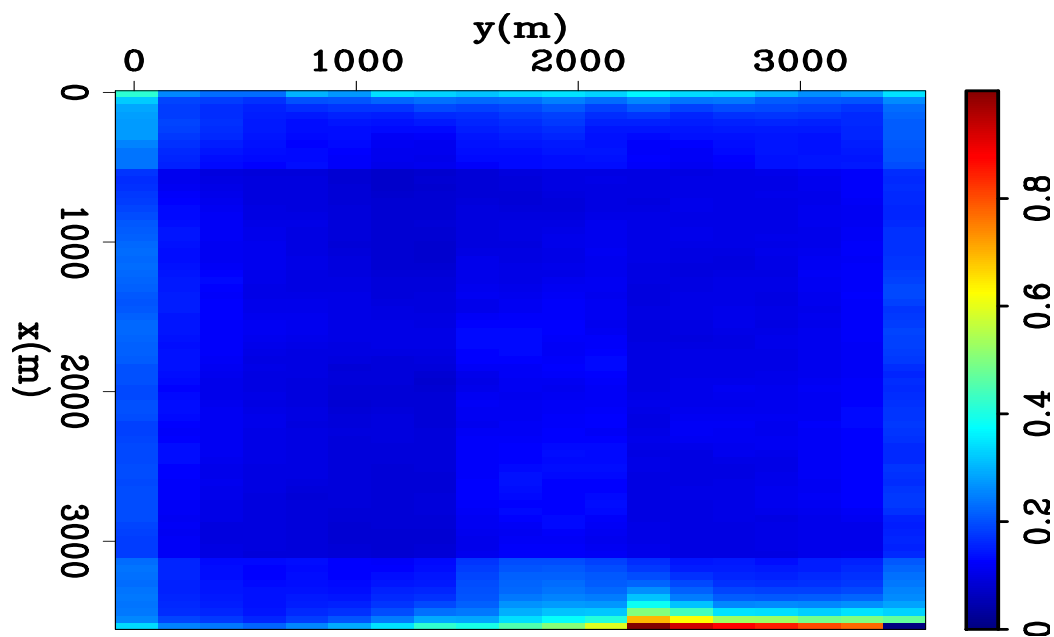


Figure 5.13: Final shot gather residual map as a function of shot locations. Each shot gather residual is normalized by the number of traces within the shot. [CR]

chap5/. rdmapf

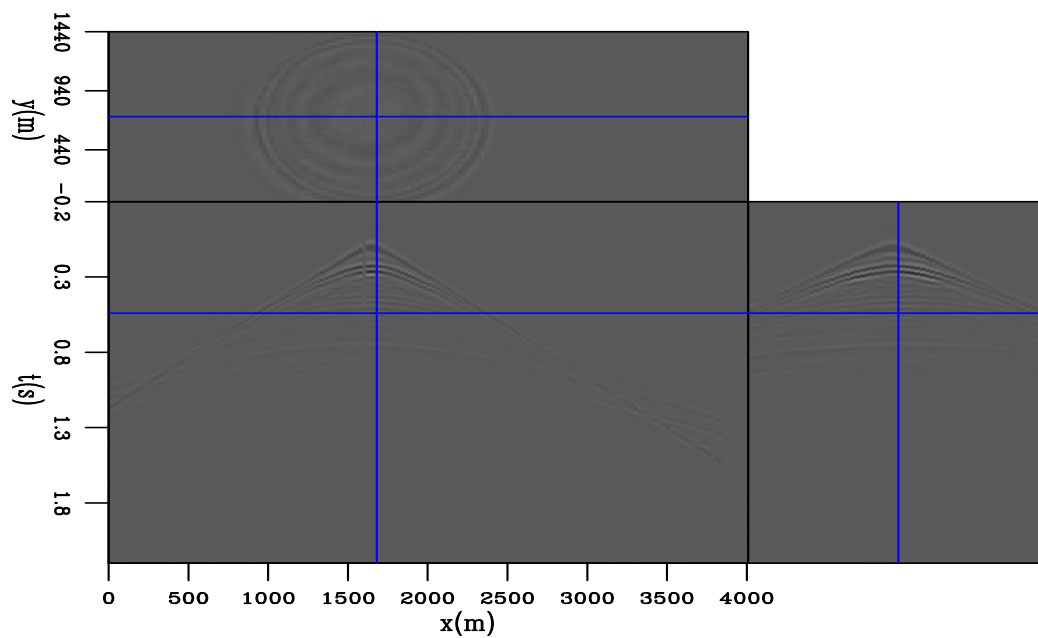


Figure 5.14: Final shot gather data residual using the input data with no band-pass.

[CR] chap5/. dresf

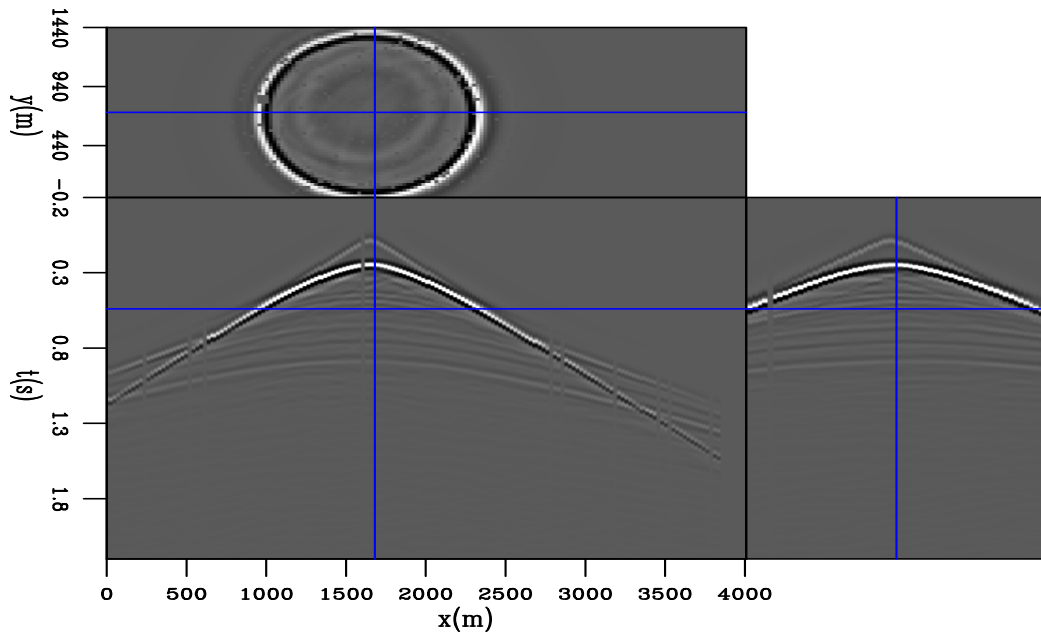


Figure 5.15: Input shot gather data with no band-pass. [CR] chap5/. dobsf

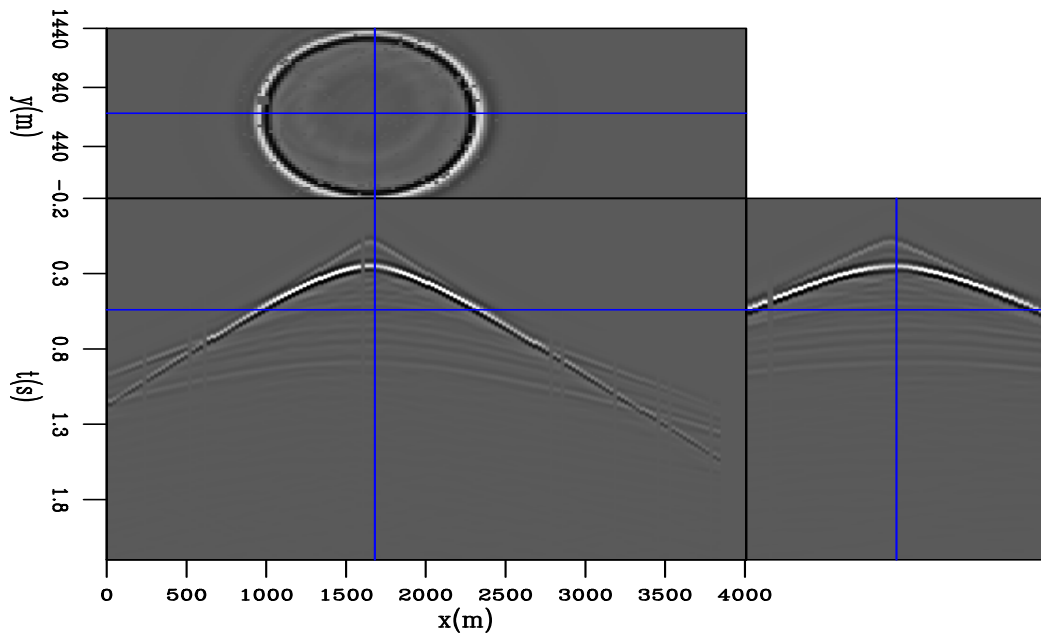


Figure 5.16: Final modeled shot gather. [CR] chap5/. dmodf

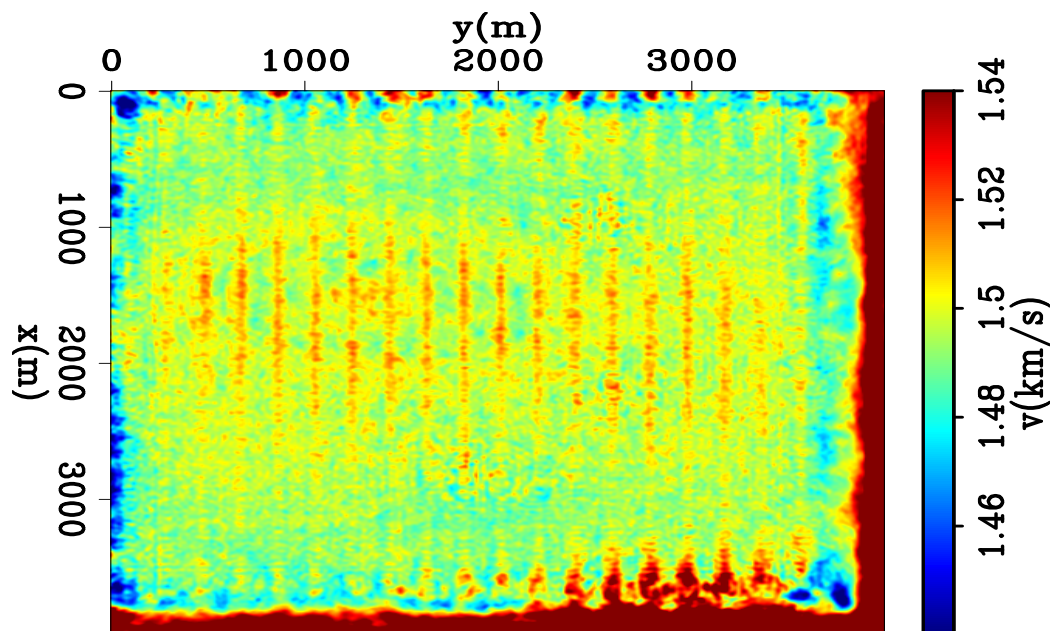


Figure 5.17: Final first layer velocity map at 80 m depth, true velocity value is 1.49 km/s for the first layer. [CR] chap5/. watervf

FIELD DATA INVERSION

In this section, I apply the same methodologies to a 3D land dataset acquired in Brazil. The entire survey was acquired in an area with rugged topography (Figure 5.18), some natural obstructions and urban activities. This environment leads to the uneven shot density (Figure 5.22), and the corresponding uneven fold distribution of the data set (Figure 5.20). The fold values range from zero to more than 200, and have significant lateral variance. For each shot, the receiver offsets range from -1.3 km to 1.3 km in the inline direction, and -900 m to 900 m in the crossline direction (Figure 5.24). For kinematic waveform inversion, I chose a portion of the dataset where the fold values are high and evenly distributed in space (Figure 5.21). The chosen area is 4 km by 2.6 km, with even source and receiver distributions (Figure 5.23). The topography is relatively flat in the chosen area, except for some valleys near the edges (Figure 5.19).

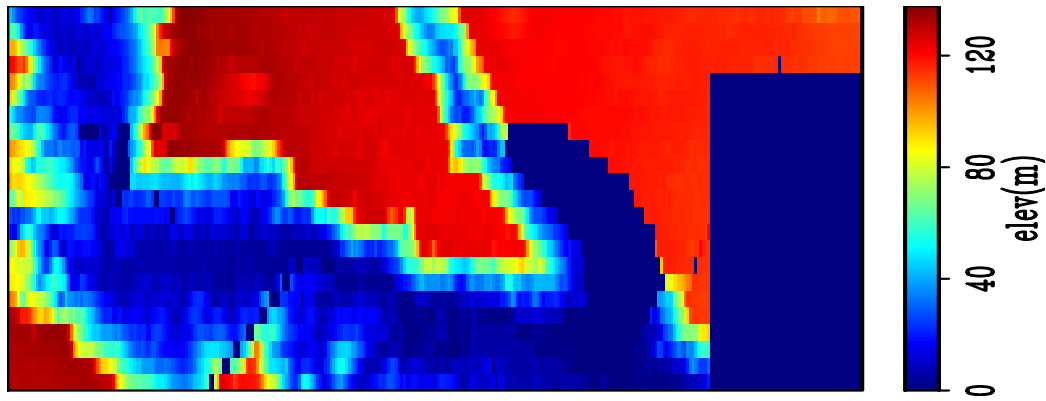


Figure 5.18: Topography (in meters) of the entire survey in reference to sea level.

[NR] chap5/. topoall

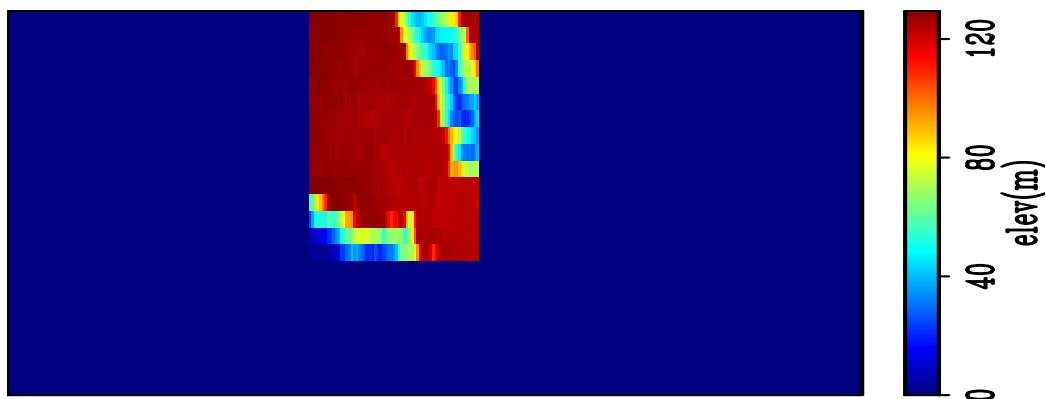


Figure 5.19: Topography of the area for inversion. [NR] chap5/. topo

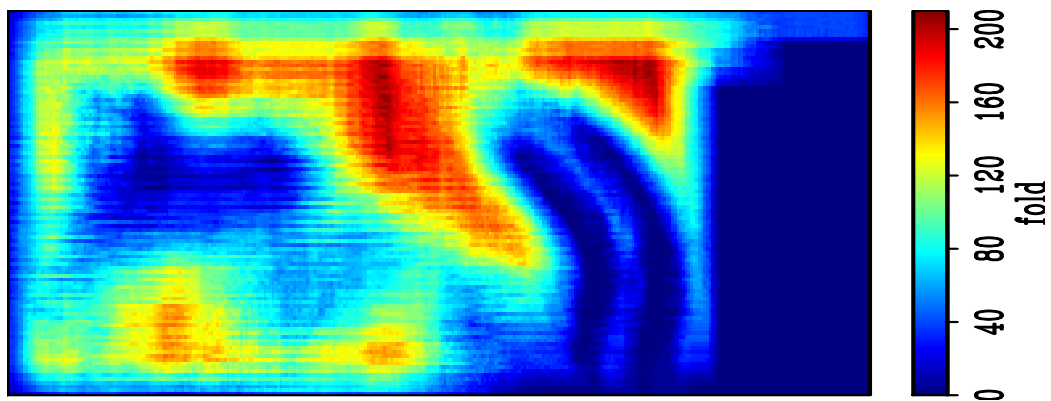


Figure 5.20: CMP fold of the entire survey. [NR] chap5/. cmpfoldall

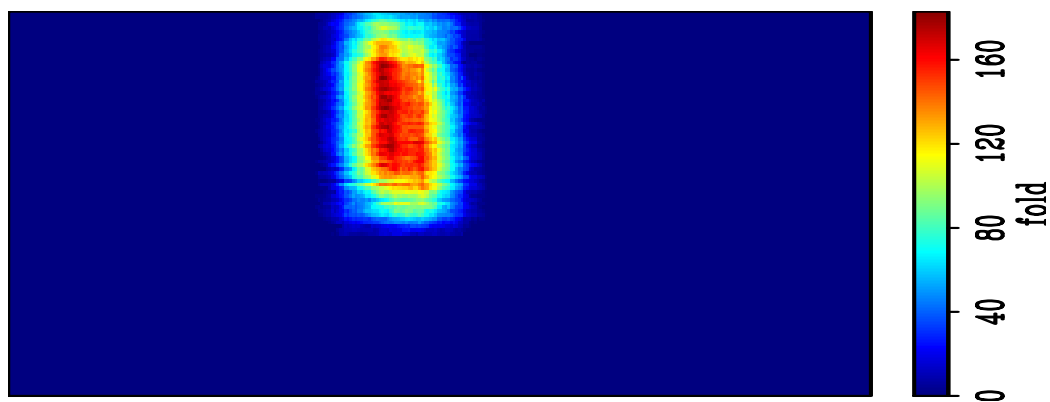


Figure 5.21: CMP fold of the data subset for inversion. [NR] chap5/. cmpfold

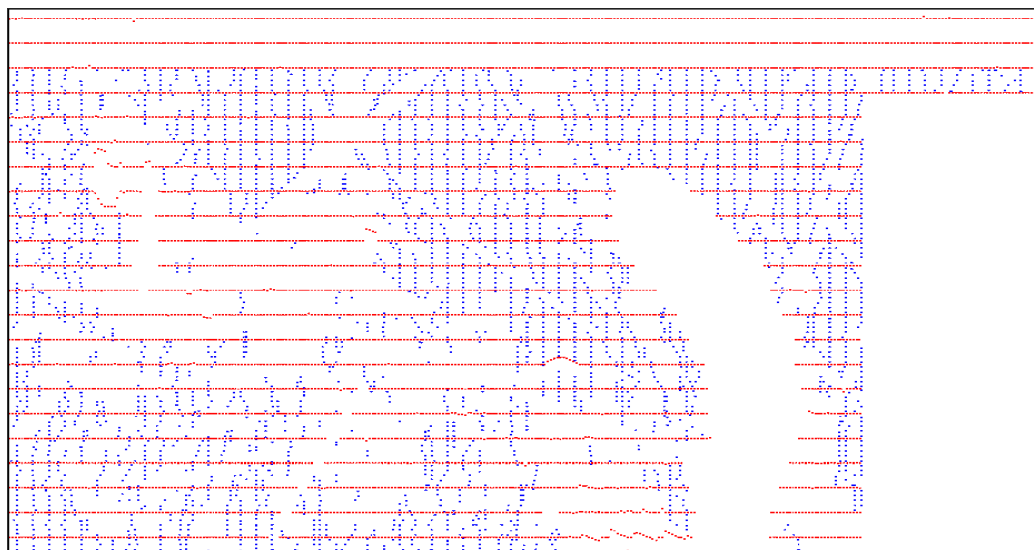


Figure 5.22: Source and receiver locations of the entire survey. Yellow dots indicate source locations, blue dots indicate receiver locations. [NR] chap5/. sgxyall

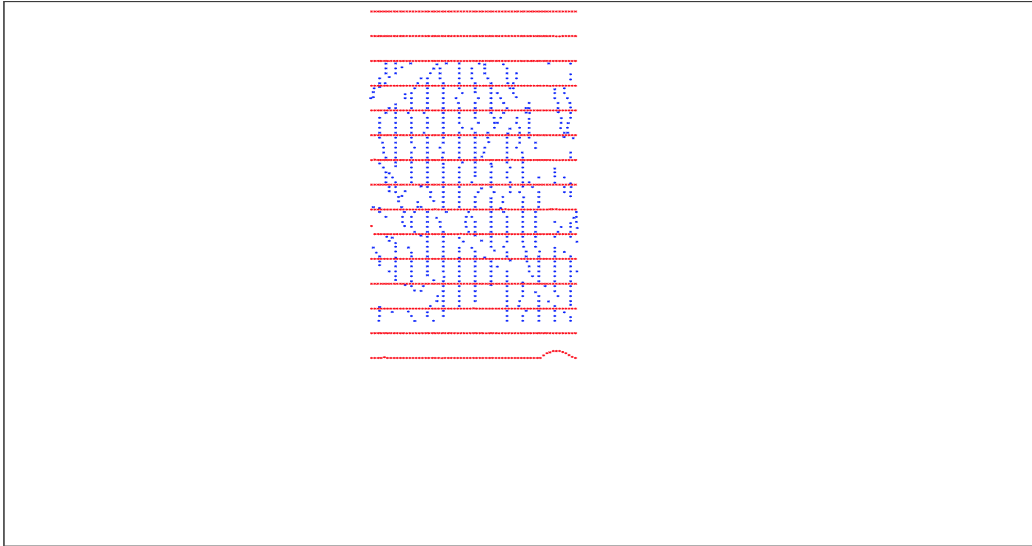


Figure 5.23: Source and receiver locations of the data subset for inversion. Yellow dots indicate source locations, blue dots indicate receiver locations. [NR] chap5/. sgxy

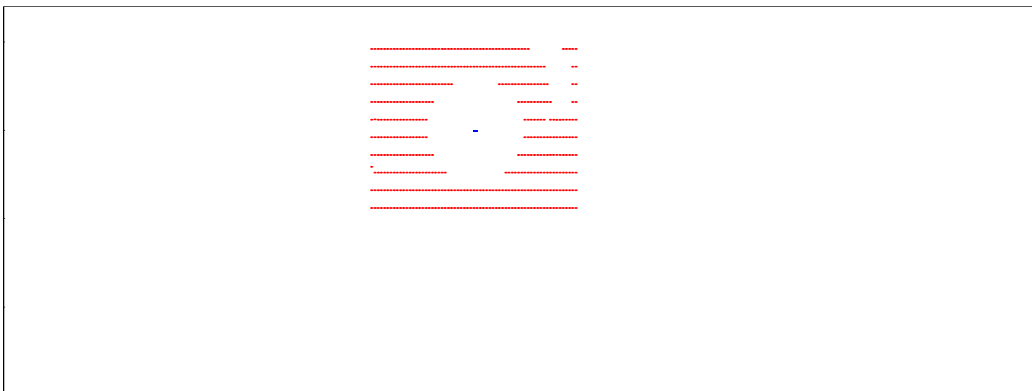


Figure 5.24: Source and receiver locations of a single shot gather. Yellow dot is the source location, blue dots are receiver locations. [NR] chap5/. sgxyoneshot

The data was minimally preprocessed to preserve the phase and the amplitude. Since dynamites were used as sources, no deconvolution was needed. The only general preprocess before the inversions is spike de-noise. And the inversion-specific preprocessing only includes bandpass, spatial and temporal windowing. Spatial windowing was applied first, where the near offsets were discarded due to the strong contamination by ground rolls and other noise (Figure 5.25 and 5.26). After that, bandpass with two different sets of parameters was applied for data used in the traveltine inversion and the kinematic waveform inversion, respectively. Data with lower frequency content were used for the kinematic waveform inversion (Figure 5.27(a) and 5.27(b)). Following bandpass, time windows were used to select the early-arrivals for the inversions (Figure 5.28(a) and 5.28(b)).

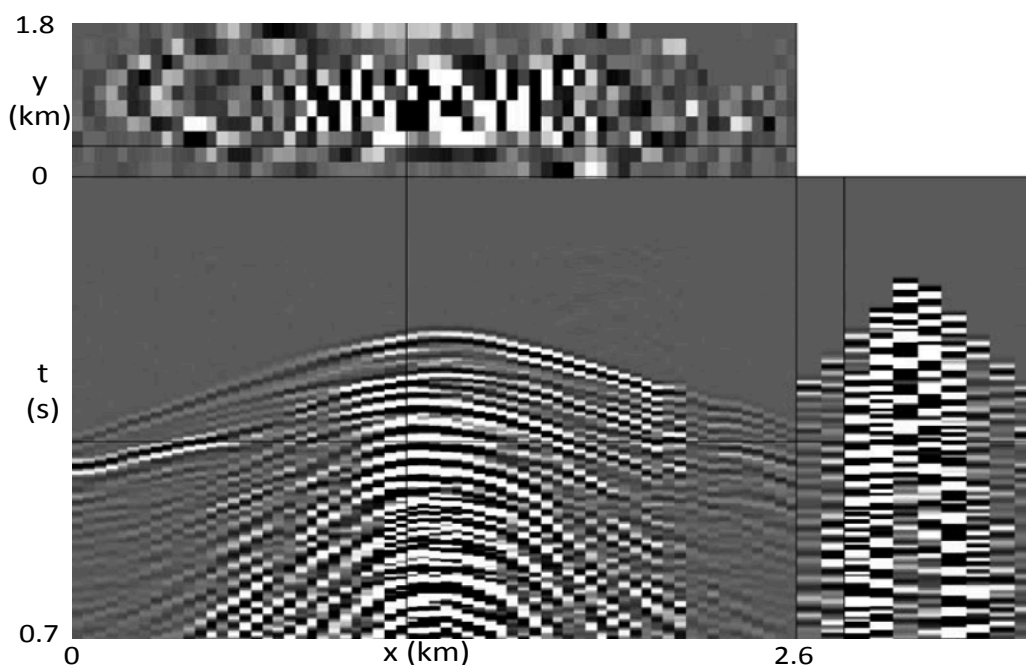


Figure 5.25: Typical shot gather after preprocessing. [NR] chap5/. dobsin

The initial model of the survey area was derived through a ray based tomography. The ray tomography result has 100m spacing in x and y, and 10m spacing in z (Figure 5.29(a)). For inversions, the ray tomography result was interpolated onto a grid of 10m spacing in x, y and z directions (Fig 5.29(b)). Thanks to the smoothness of the

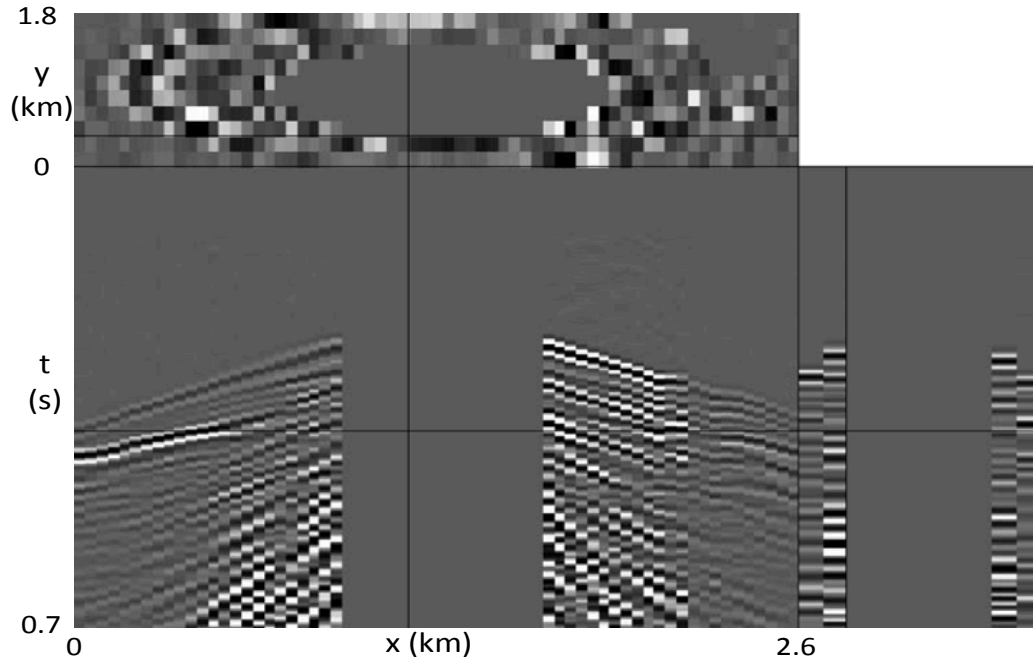


Figure 5.26: The same shot gather after near offset muting. [NR]
 chap5/. nrofstmute

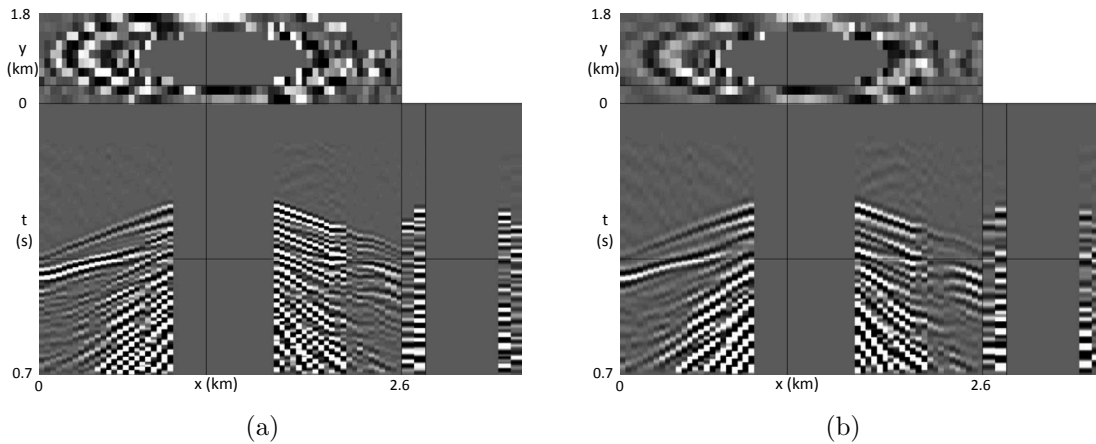


Figure 5.27: The near-offset muted shot gather after bandpassing. a) Bandpassed for the traveltime inversion; b) Bandpassed for the kinematic waveform inversion. [NR]
 chap5/. bandpasswt,bandpasswi

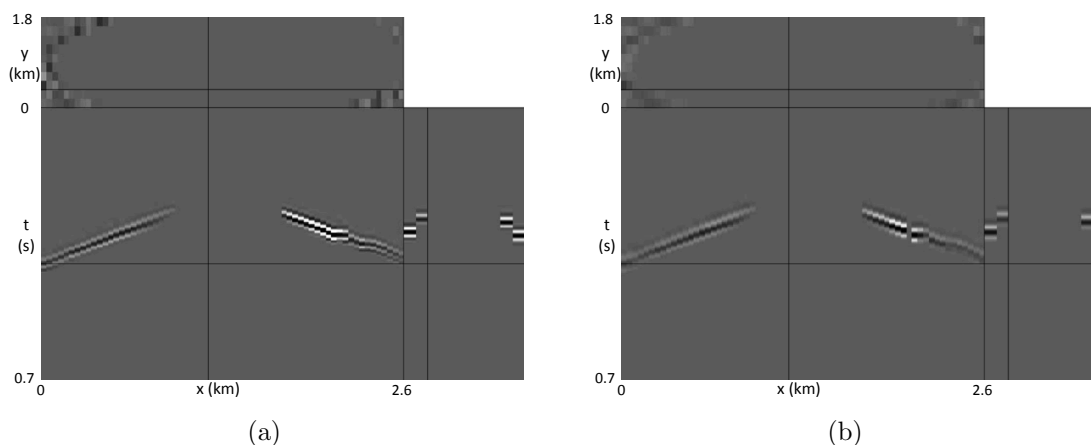
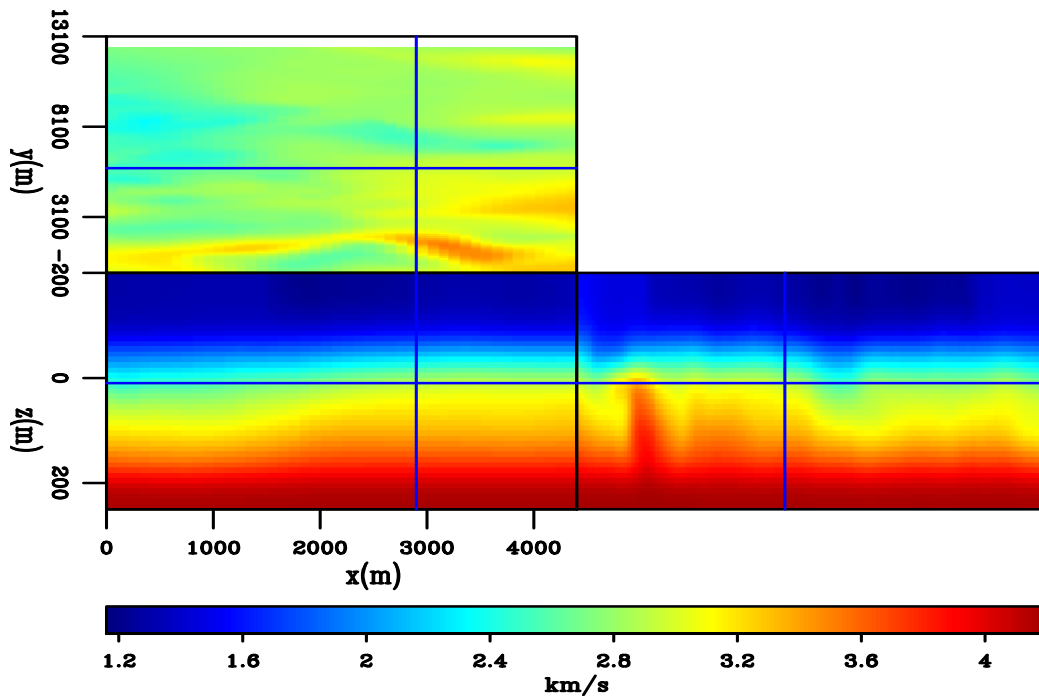


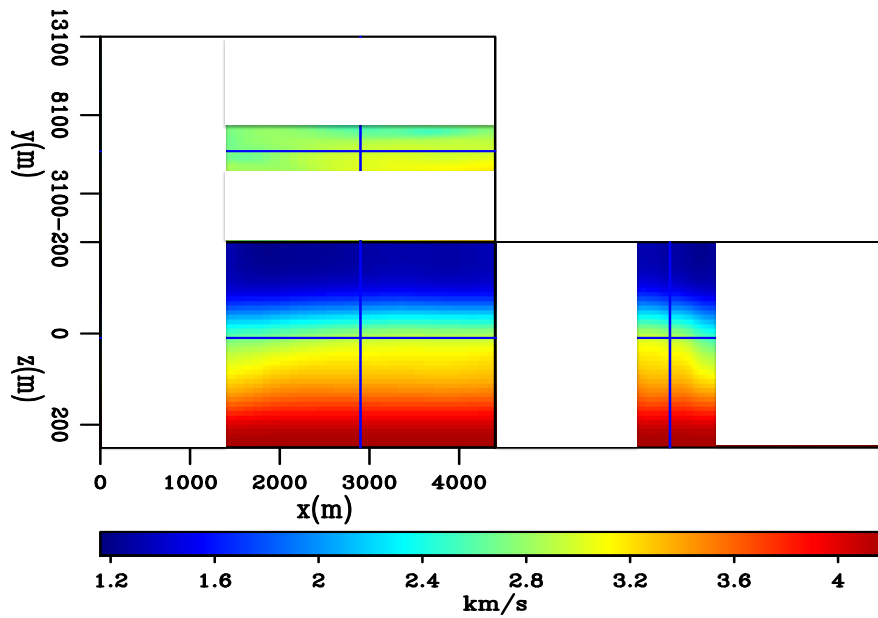
Figure 5.28: The near-offset muted and band-passed shot gather after time windowing. a) Time windowed for the traveltime inversion; b) Time windowed for the kinematic waveform inversion. [NR] chap5/. eamutewt,eamutewi

ray tomography result, interpolation did not result in any artifact. As mentioned before, elevations are non-trivial in the area, so the velocity model starts from 200m above sea level. This ensures that all the sources and receivers sit within the model. The source and receiver elevations were rounded to the nearest grid points. Given that the velocity below the sources and receivers (≈ 1.15 km/s) is fast for very shallow near-surface environment, this rounding produces a vertical traveltime error of 4 ms at most. To put this in perspective, the traveltime inversion has a dominant data period of 40 ms, and the kinematic waveform inversion has a dominant data period of 60 ms. Hence, the errors in the source/receiver elevation round up has very little impact on the traveltime inversion, and even less impact on the kinematic waveform inversion.

From the initial model, I generated synthetic early-arrivals and compared them with the observed early-arrivals (Figure 5.30). In each plot in the figure, 3D shot gathers were displayed as 2D by concatenating different crossline slices of the shot gather next to each other, the discontinuity of the first-break indicates where crossline slices jump from one to the next. For this particular shot gather, as well as the ones in the following 2D displays of 3D gathers, the source location is on the left edge of the



(a)



(b)

Figure 5.29: Initial velocity for a) the entire survey area; b) the inversion area. [NR]

chap5/. fdvinitall,fdvinitcrop

third crossline slice from the left. The traveltimes errors in the near-offset are small, which indicate good velocity model in the shallow part of the near-surface. The large traveltimes errors mainly exist at the far offset (Figure 5.32 blue curve), suggesting poorer velocity estimation in the deeper parts of the near-surface model. Since the far offset traveltimes errors are larger than the dominant period of the data, the ray-tomography result is not a good enough starting model for the kinematic waveform inversion. To overcome this, I applied the two-step workflow described in chapter 2, where I apply wave-equation traveltimes inversion first, followed by the kinematic waveform inversion.

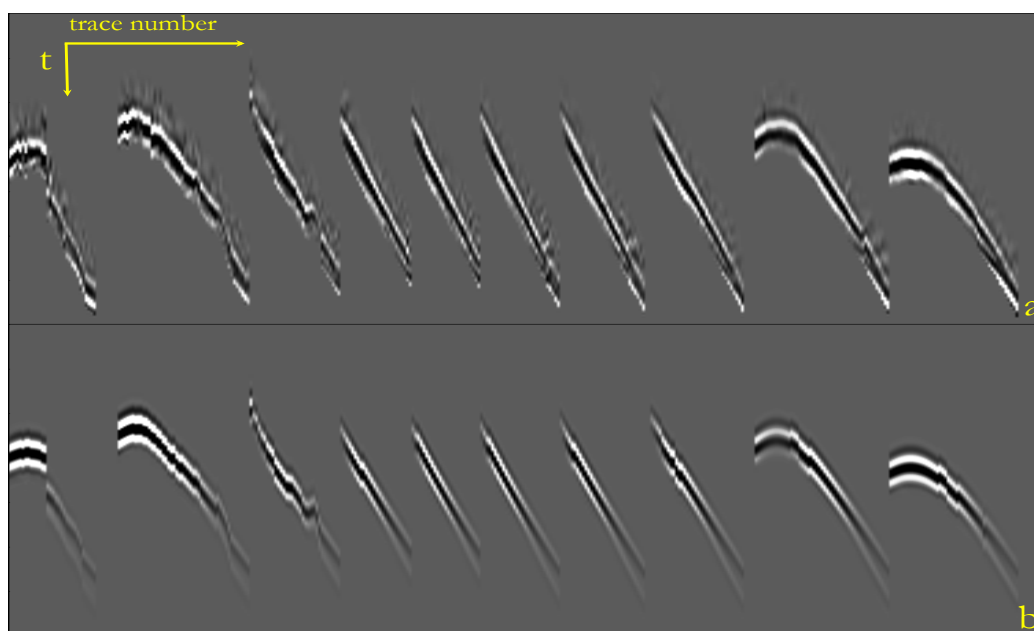


Figure 5.30: 2D display of 3D: a) Observed early-arrivals; b) Modeled early-arrivals from the initial model for traveltimes inversion. [NR] chap5/. wtmodc

A total of 10 iterations were run for the wave-equation traveltimes inversion. Such small number of iterations comes from the large steplength used during each iterations. The choice of large steplength is due to the fact that, in contrary to the waveform errors, the traveltimes errors behave more linear with respect to the velocity errors. The traveltimes inversion was able to reduce the objective function value

significantly (Figure 5.31), down to less than 10% of the initial value. The cycle skipping at the far offsets become much smaller than the dominant period of the data for kinematic waveform inversion (Figure 5.32 red curve). The average traveltimes error approaches zero, which suggests that the traveltimes inversion result has the correct long-wavelength component. First-breaks of different offset travel through different depth of the near-surface model, larger offset first breaks travel through deeper parts of the near-surface model. As a result, the initial traveltimes errors at the far offsets reflect poor velocity in the middle and deep part of the near-surface model. This is reflected in the traveltimes inversion result where the velocity in the middle and deep parts of the model become significantly slower compared to that of the initial model (Figure 5.33 and 5.34).

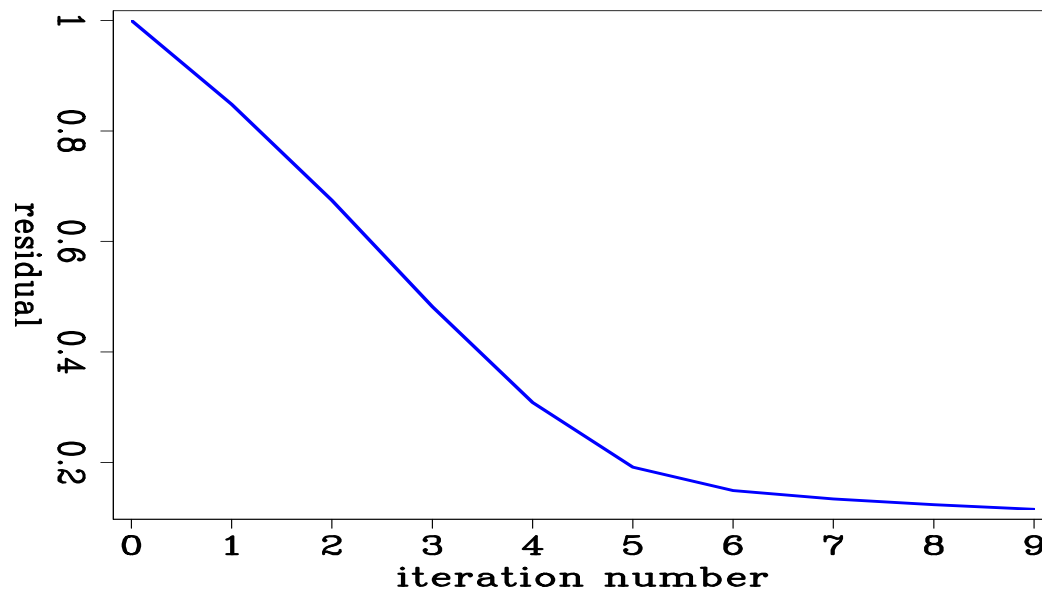


Figure 5.31: Objective function values as a function of iterations for the first-break traveltimes inversion. [NR] `chap5/.fdresdwt`

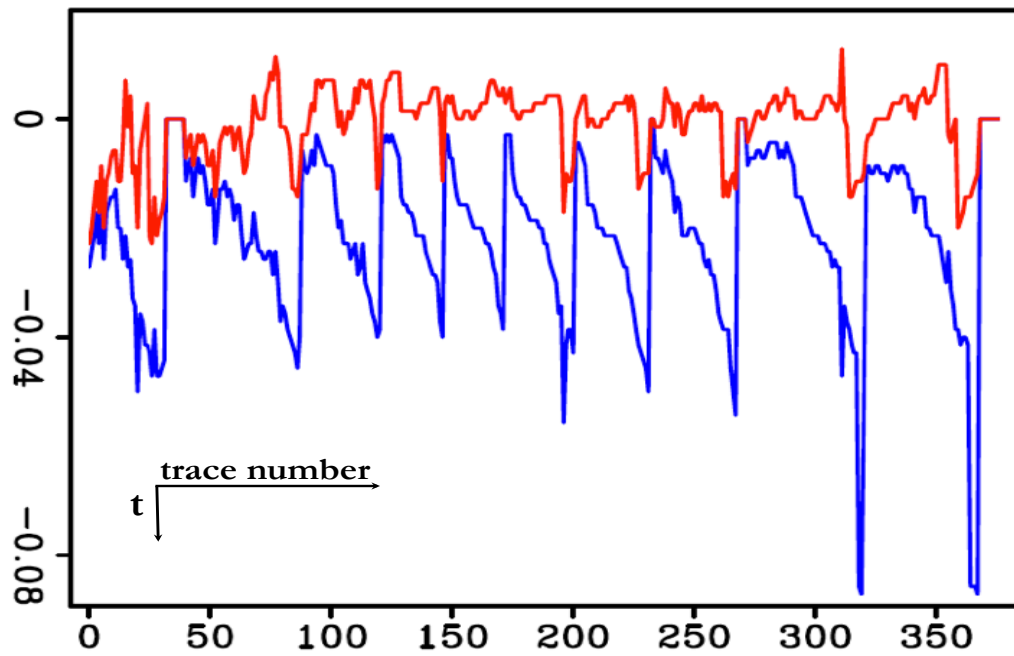


Figure 5.32: 2D display of 3D shot gather traveltimes residuals, blue: before the travel-time inversion; red: after the travel-time inversion. [NR] chap5/. wtrdful

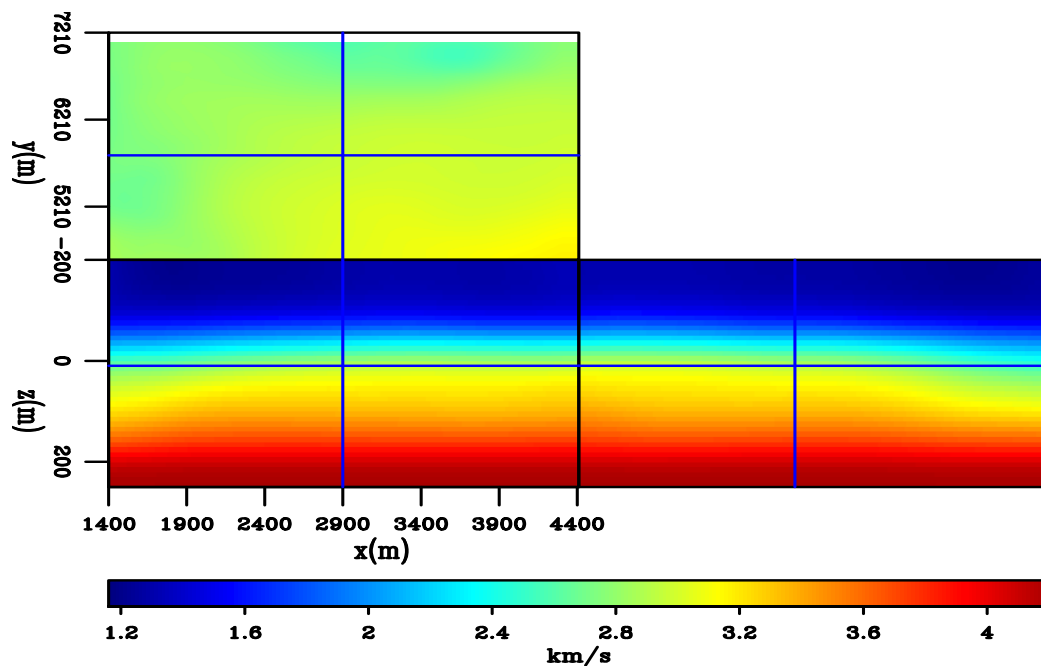


Figure 5.33: The initial velocity for the inversions. [NR] chap5/. fdvinit

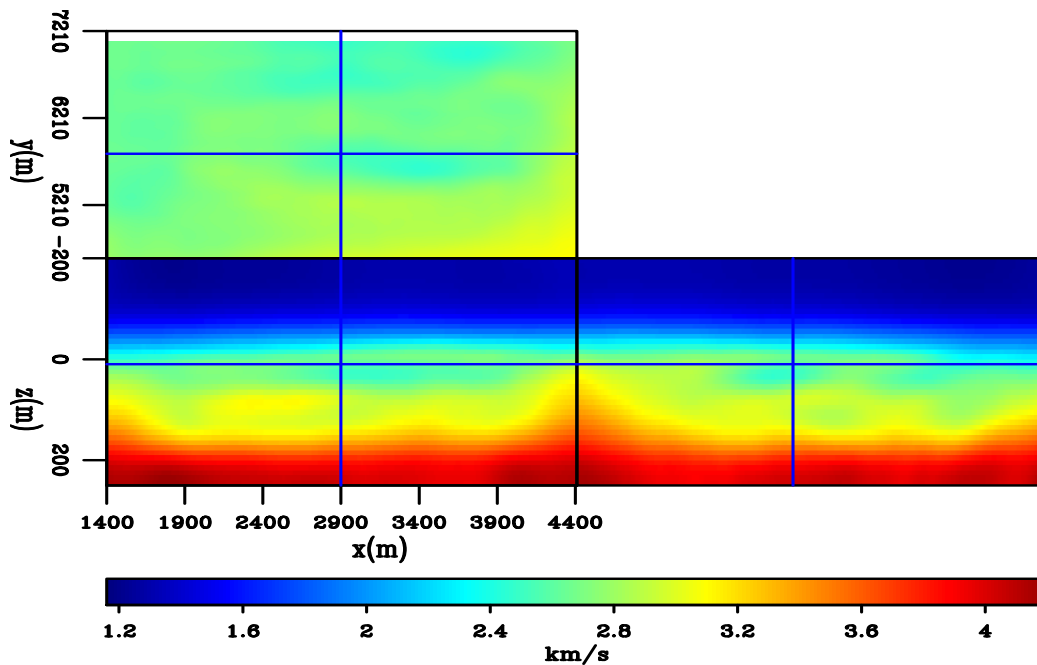


Figure 5.34: The velocity model from the travelttime inversion. [NR]
 chap5/. fdvinvwt

After the travelttime inversion, kinematic waveform inversion was performed, with lower frequency observed data than those used for the travelttime inversion. A total of 20 iterations were run (due to time and computational constraints during the internship at Petrobras), using only the observed first-breaks as early-arrivals. The kinematic waveform inversion result has more details and lateral variations compared with the travelttime inversion result (Figure 5.35), especially in the middle and deep part of the model where the previous travelttime inversion significantly reduced the travelttime errors yet could not completely eliminate them. This is reflected in the data matching after the kinematic waveform inversion (Figure 5.38), where the middle and far offset data residuals were reduced more than the near-offset data residuals. Overall, the kinematic waveform inversion reduced the initial objective function value by more than 60% (Figure 5.36), which is significant reduction given only the first-break is used. Furthermore, the behavior of the objective function suggests further reduction of the objective function value is likely if I had more time to run more

iterations. Putting the kinematic waveform inversion result into the initial velocity model of the entire area, it is obvious that the inversion workflow not only corrected the long-wavelength model errors, but also resulted in a final model of much higher resolution compared with the ray-based tomography result (Figure 5.37).

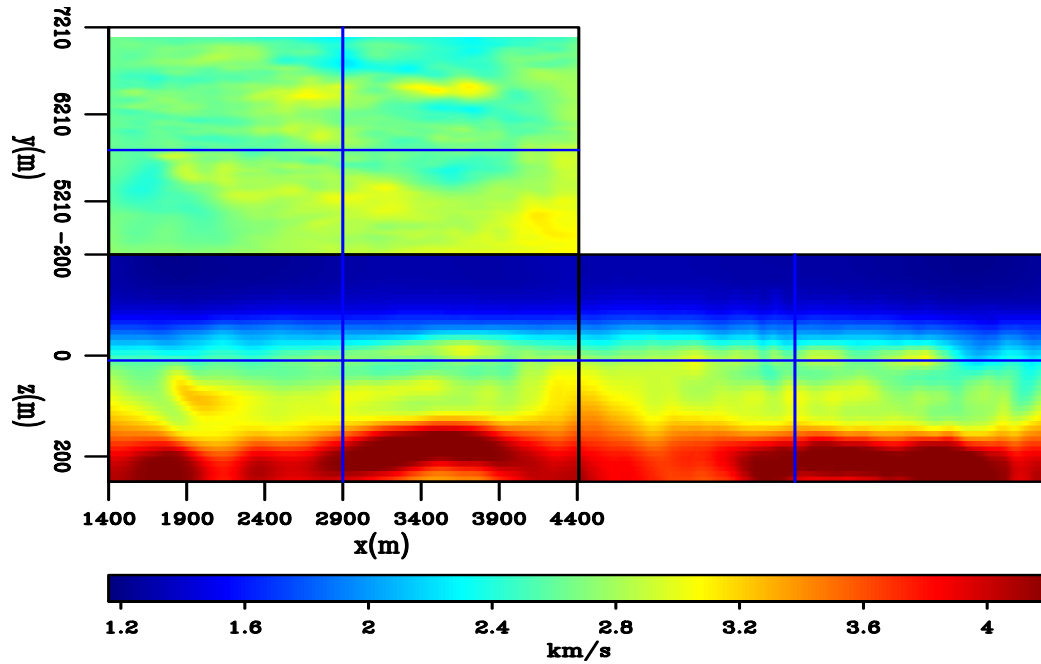


Figure 5.35: The velocity model from the kinematic waveform inversion. [NR]
 chap5/. fdvinvwi

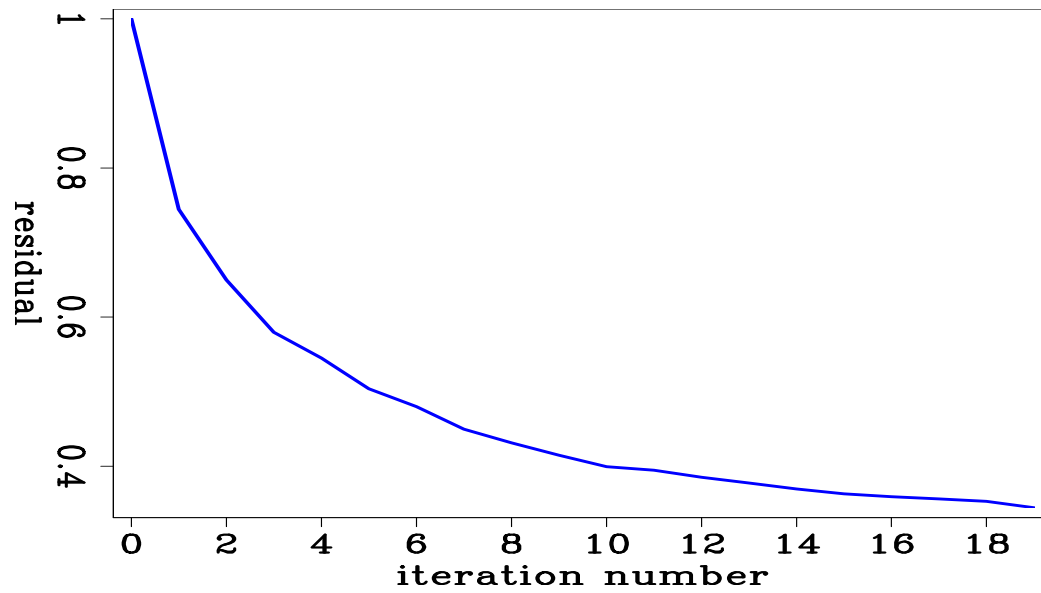


Figure 5.36: Objective function values as a function of iterations for the kinematic waveform inversion. [NR] chap5/. fdresdwi

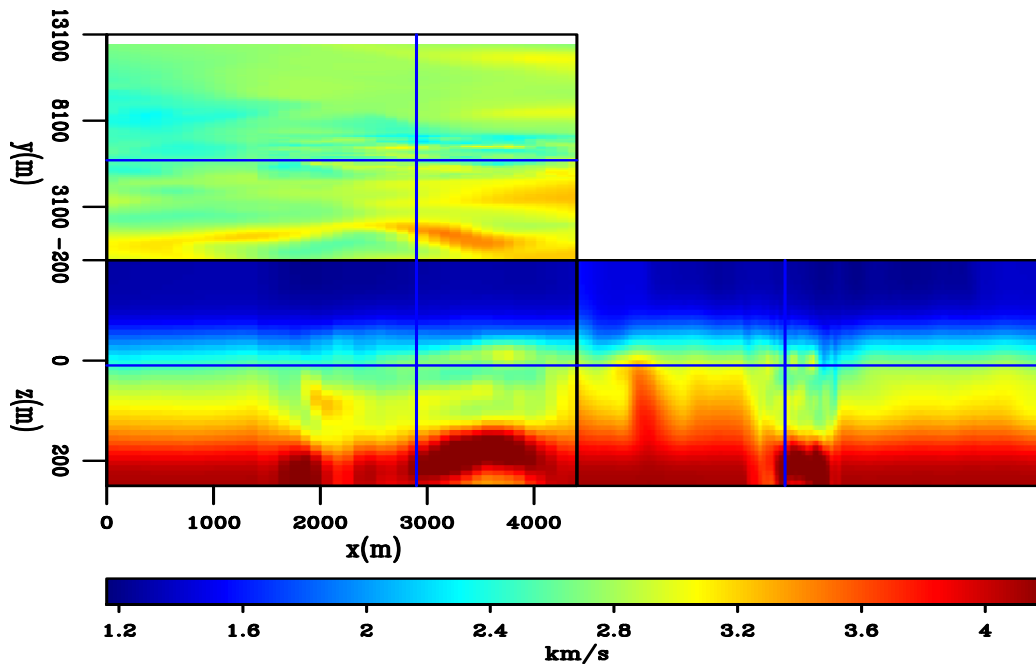


Figure 5.37: The final inversion result put back into the initial model of the entire area. [NR] chap5/. fdvinvcat

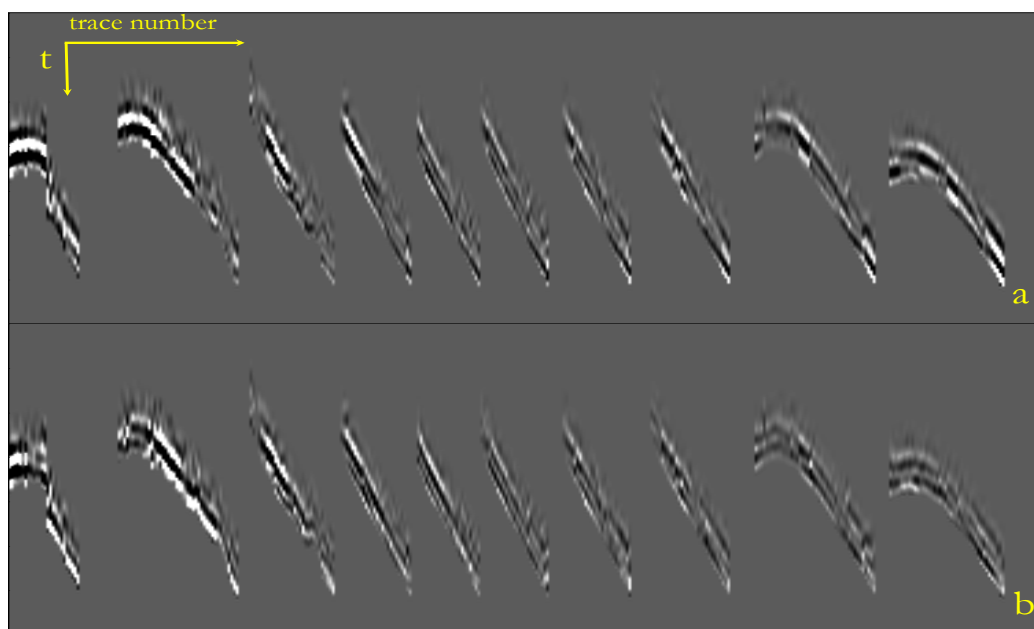


Figure 5.38: 2D display of 3D shot gather kinematic waveform residual, a: before the inversion; b: after the inversion. [NR] chap5/. wurdful

CONCLUSIONS

The methodologies developed in the previous chapters enable practical applications of the waveform inversion. The starting models can be obtained by applying early-arrival wave-equation traveltimes inversions. Such starting models can then be used for early-arrival kinematic waveform inversions to obtain high-resolution near-surface models. In the area illuminated by early-arrival wave-equation traveltimes inversions, the final result not only has the correct long-wavelength components, but also reveals details of the models that ray-based tomography cannot recover. These advantages of the waveform inversion methodologies developed in the previous chapters were verified by the 3D synthetic and field data results.

ACKNOWLEDGMENTS

I would like to thank Robert Clapp for generating the synthetic model and data for the synthetic inversion. I would also like to thank Petrobras for allowing me to work on the 3D land dataset and publish the results in this chapter.